

Microtextural constraints on the interplay between fluid–rock reactions and deformation

Alexis K. Ault · Jane Selverstone

Received: 31 August 2007 / Accepted: 17 March 2008 / Published online: 29 March 2008
© Springer-Verlag 2008

Abstract Schists from two mylonitic localities in the footwall of a low-angle normal fault in the eastern Alps record different degrees of embrittlement during exhumation, depending on the extent to which fluid–rock reactions proceeded. At one site, graphitic schists preserve textural evidence for two metamorphic reactions that modified X_{CO_2} and/or fluid volume: (1) reaction between graphite and aqueous fluid that increased X_{CO_2} without changing the molar amount of fluid, and (2) replacement of titanite by rutile, calcite, and quartz. The latter reaction involved net consumption of increasingly CO_2 -rich fluid. Areas where the first reaction proceeded are associated with abundant Mode I microcracks. Fluid inclusion arrays within the microcracks show that X_{CO_2} increased from ~ 0.1 to 0.6 during decompression from 4.75 to 2 kbar at a reference temperature of 500°C. Titanite consumption is most pronounced within transgranular Mode I microcracks, but microcracks do not crosscut products of this reaction; fluid consumption during reaction was coeval with the end of microcracking, at least on a local scale. At the other site, graphitic schists lack small-scale Mode I cracks as well as evidence for graphite consumption during decompression. SEM imaging shows that graphite is anhedral and pitted at

the first site, but occurs in clusters of euhedral grains at the second site. Mass balance calculations demonstrate that rocks with partially consumed graphite were infiltrated by an externally derived, H_2O -rich fluid that drove subsequent graphite–fluid reaction. Evidence for similar fluid infiltration is absent at the second site. Variations in the degree of reaction progress indicate that fluid pathways and deformation style were heterogeneous on the scale of millimeters to kilometers during exhumation from mid-crustal depths.

Keywords Alps · Fluid–rock reaction · Graphite · Titanite · Carbonic fluid · Embrittlement

Introduction

Any rock that contains hydrous minerals along with carbonate \pm graphite has the potential to evolve a mixed C–O–H fluid during metamorphism, and numerous papers have explored the chemography of the resulting fluid–rock reactions (e.g. French 1966; Ohmoto and Kerrick 1977; Bowers and Helgeson 1983; Connolly and Trommsdorff 1991; Connolly and Cesare 1993). Metamorphic decarbonation \pm graphite-consuming reactions have been invoked to explain CO_2 -rich fluids in shear zones (Selverstone et al. 1995; Wawrzyniec et al. 1999; Axen et al. 2001), degassing of CO_2 in collisional and extensional orogens (Kerrick and Caldeira 1993a, b; Selverstone and Gutzler 1993; Nesbitt et al. 1995), and CO_2 overpressure resulting in seismicity (Colletini et al. 2000; Colletini and Barchi 2002; Chiodini et al. 2004; Miller et al. 2004). Likewise, many studies have called upon infiltration of externally derived carbonic fluids to explain graphite precipitation in deep shear zones (Radhika and Santosh 1996;

Communicated by T.L. Grove.

A. K. Ault (✉) · J. Selverstone
Department of Earth and Planetary Sciences,
University of New Mexico, MSC03 2040,
Albuquerque, NM 87131-0001, Mexico
e-mail: alexis.ault@colorado.edu

Present Address:

A. K. Ault
Department of Geological Sciences,
University of Colorado at Boulder,
2200 Colorado Ave, Boulder, CO 80309, USA

Binu-Lal et al. 2003; Bigalke et al. 2004). However, few studies have documented textural evidence for specific reactions associated with changing fluid composition, particularly those involving graphite consumption, or have considered the possible interplay between fluid–rock reactions and deformation.

Selverstone (2005) noted a correlation between the presence of graphite, Mode I microfractures, and carbonic fluid inclusions from several localities in the Tauern Window, Eastern Alps. Samples lacking graphite contained only aqueous fluid inclusions and showed no Mode I cracks. Selverstone inferred that interaction between graphite and an aqueous fluid locally increased X_{CO_2} , leading to greater pore fluid expansion during decompression relative to samples in equilibrium with an aqueous fluid. The resulting pore fluid overpressure caused preferential brittle failure and formation of extension fractures in the graphitic horizons.

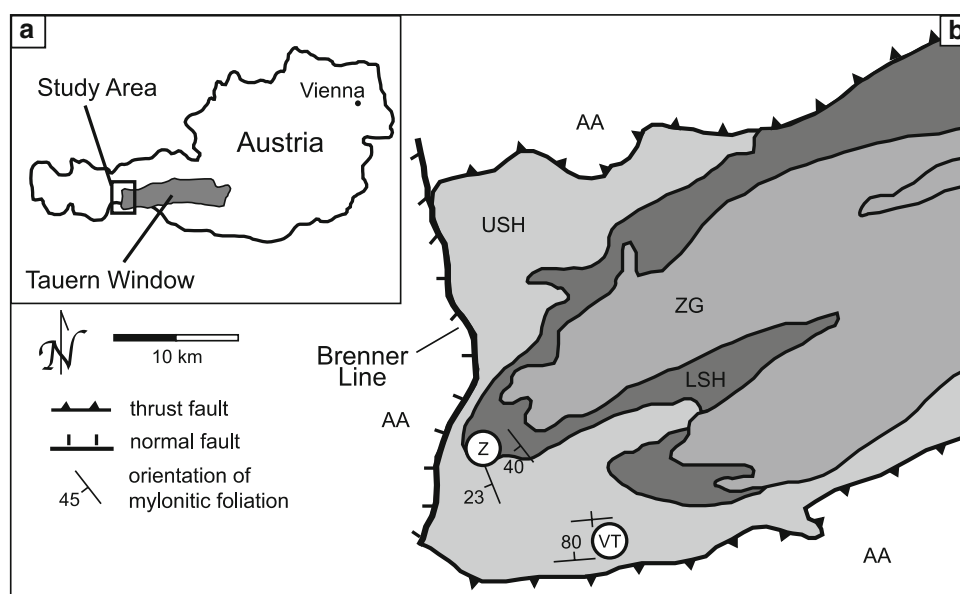
The observations and interpretations of the Selverstone (2005) paper suggest that heterogeneities in fluid composition can be generated and preserved on small scales during metamorphism, and that these heterogeneities can play an important role in controlling strain accommodation mechanisms during orogenesis. In particular, local generation of carbonic fluids via metamorphic reactions may contribute to rock embrittlement, even at elevated pressures and temperatures, via several mechanisms: (1) inhibiting dislocation climb by reducing f_{H_2O} (Post et al. 1996), (2) inhibiting dissolution-precipitation creep by reducing the solubility of quartz (Newton and Manning 2000), and (3) increasing pore fluid pressure via preferential expansion of carbonic fluids relative to aqueous ones during decompression (Selverstone 2005).

Intercalated graphitic and non-graphitic calc-mica schists in the footwall of the Brenner low-angle normal shear zone along the western margin of the Tauern Window, Eastern Alps (Fig. 1), provide an excellent opportunity to document possible fluid–rock interactions involving mixed C–O–H fluids. In this study, we look in detail at the grain-scale evidence for fluid–rock reactions and the spatial relationships between reaction textures and microcracks at two localities in the same general region as the Selverstone (2005) study. Both localities developed mesoscale extension fractures during unroofing, but only one of the sites shows evidence for extensive sub-millimeter-scale microcracking and fluid–rock reaction. The main goal of this work is to use microtextural and chemical data to document the relationships, if any that exist between mechanical behavior of the rocks and specific reactions that affected fluid composition and/or amount.

Tectonic setting

Continent–continent collision in the Alps began in the latest Cretaceous and continued into the mid-Tertiary with the closure of the Alpine Tethys ocean and the southward subduction of the European continent beneath the Adriatic plate (e.g. Stampfli et al. 2002). Orogenesis resulted in the deep burial of the Pennine nappes in the Tauern Window beneath the allochthonous Austroalpine nappe sequence (Fig. 1; Selverstone et al. 1984; Lammerer 1988). The Pennine units include three lithotectonic packages (Fig. 1; e.g. Morteani 1974): the Zentralgneis (ZG), composed of Paleozoic granitic intrusions; the Lower Schieferhülle (LSH), autochthonous Paleozoic schists and amphibolites

Fig. 1 **a** Location of the Tauern Window and area of study with respect to Austria. **b** Simplified geologic map of the southwest corner of the Tauern Window near the Brenner Line detachment. Penninic basement units: ZG Zentralgneis, LSH Lower Schieferhülle, and USH Upper Schieferhülle. AA Austroalpine nappes in hanging wall of the detachment. Sample localities: VT Vals Tal and Z Zirogalm



and Mesozoic para-autochthonous shallow marine sediments; and the Upper Schieferhülle (USH), metamorphosed Mesozoic rocks of the Alpine Tethyan ocean basement.

Concomitant orogen-parallel extension and exhumation of mid-crustal rocks was accommodated in part by slip on the north-south trending Brenner Line low-angle detachment that bounds the western margin of the Tauern Window (Behrmann 1988; Selverstone 1988; Axen et al. 1995; Fügenschuh et al. 2000). The extensional mylonitic foliation in the footwall strikes approximately east–west and generally dips shallowly to moderately to the WSW, passing into a region of subvertical dips along the southern margin of the Tauern Window (Fig. 1). The foliation is overprinted by synthetic (west-down) and antithetic (east-down) semi-brittle and brittle structures (Axen et al. 1995). Ductile shearing and brittle faulting were contemporaneous at depths of 15–20 km and temperatures in excess of 400°C (Selverstone et al. 1995). In the areas of this study (Fig. 1), calc-mica schists contain abundant west-side-down, high-angle normal faults, and some horizons additionally display micro- and meso-scale Mode I fractures.

Field observations, mineral chemistry, and reaction textures

Graphitic and non-graphitic calc-mica schists were sampled along two transects in the footwall of the Brenner Line (Fig. 1) in order to explore relationships between fluid–rock reactions and development of post-mylonitic (but syn-metamorphic) brittle structures. Both localities display abundant post-mylonitic extension fractures in the field (Fig. 2). However, the two localities are in different structural positions within the Tauern Window, show significantly different abundances of microscopic Mode I cracks, and preserve evidence for different degrees of fluid–rock reaction. The first transect is along the southern border of the Tauern Window in Upper Schieferhülle rocks of the Vals Tal. Rocks in this area are steeply overturned to the north, reflecting transpressive motion between Europe and the Adriatic plate during east–west extension and exhumation of the Tauern Window (e.g. Stöckli 1995; Mancktelow et al. 2001). The second transect cuts obliquely across a dip slope of the Mesozoic Lower Schieferhülle immediately beneath the Brenner Line detachment near the village of Zirogalm in the western part of the window. The mylonitic foliation here dips gently towards the west and is cut by abundant brittle-ductile shears and both east- and west-down brittle structures related to movement of the footwall through the Brenner Line rolling hinges (Axen et al. 1995). In contrast, the Vals Tal locality lies to the east of the region affected by these structures. At both sites, extension fractures such as those

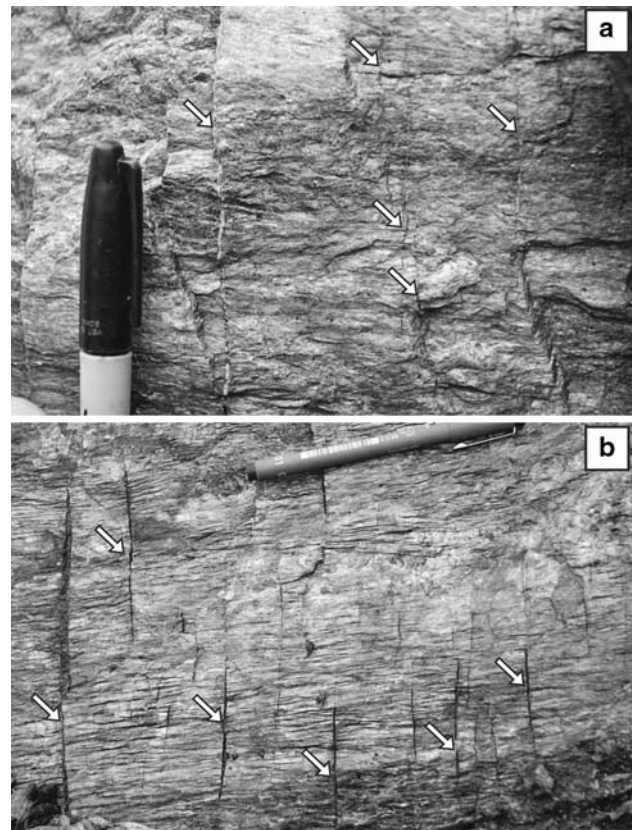


Fig. 2 Field photographs showing spaced Mode I fractures (denoted with *white arrows*) in graphitic schists from the two study sites. **a** Vals Tal, looking N at subvertical foliation surface. **b** Zirogalm, looking down on gently W-dipping foliation surface

shown in Fig. 2 are present, but in the Vals Tal these are most abundant within graphitic layers. At the Zirogalm locality, fractures are present in both graphitic and non-graphitic schist horizons.

To supplement petrographic observations, chemical analyses of select minerals from Vals Tal samples were obtained using a JEOL 8200 electron microprobe at the University of New Mexico. The instrument was calibrated using standards of natural and synthetic materials. The microprobe was operated at 15 keV accelerating voltage and a 20 nA beam current. The beam diameter was 10 μm on plagioclase and 1 μm on all other phases. Counts were collected for 20 s on peak and 10 s on background positions; for minor elements, counts were collected for 30 s on peak and 15 s on each background position.

Vals Tal transect

Graphitic and non-graphitic schists and marbles in the Vals Tal (Fig. 1) are interlayered with one another on scales ranging from centimeters to tens of meters. In the Vals Tal, the foliation consistently strikes between 260° and 265°

and dips between 75°N and vertical; the lineation is approximately horizontal. Graphitic schists contain fractures that are oriented orthogonal to the lineation with no apparent offset (i.e. Mode I); similar fractures are noticeably absent in interlayered non-graphitic schists and marbles. Typically, these cracks are up to 15 cm in foliation-perpendicular length, 1–2 mm wide and filled with quartz ± carbonate, and spaced every 3–6 cm (Fig. 2a). Cracks present in the graphitic schists terminate at the contact with adjacent non-graphitic schist and marble, similar to the relationships described by Selverstone (2005; e.g. see Fig. 1a in that study).

Graphitic and non-graphitic schists contain similar abundances of matrix quartz, calcite, phengite, and

plagioclase and accessory clinozoisite, ilmenite, tourmaline, and chlorite. Graphitic rocks additionally contain individual porphyroblasts of plagioclase, titanite, and clinozoisite, and graphite abundance is significantly higher within these porphyroblasts than in the matrix. Rutile is also present in graphitic schists that contain titanite. Both graphitic and non-graphitic schists are intercalated with marble horizons, composed primarily of calcite, quartz, and phengite, and both contain abundant foliation-parallel quartz ± calcite layers and veins that range up to a few cm in thickness. Key phases from the graphite-bearing samples are discussed below. Representative mineral analyses for calcite, rutile, plagioclase, and titanite are presented in Table 1.

Table 1 Representative electron microprobe analyses for phases in graphitic schists

	Plagioclase		Calcite		Titanite				Rutile			
Sample	VT6b	VT6b	VT6a	VT6a	VT6a	VT6a	VT3	VT3	VT6a	VT6a	VT3	VT3
Region	1b_5	1b_6	1a_1	1a_3	1a_1	1a_4	3a_3	3a_4	1a_3	1b_2	3a_6	3a_7
	rim	core	rim, m	rim, t	core	rim	core	rim	core	core, gb	core, in crack	core, bn
SiO ₂	60.35	61.16	–	–	31.09	30.76	30.69	30.85	0.07	0.62	0.00	0.00
TiO ₂	–	–	–	–	34.24	34.86	35.87	36.23	100.06	97.59	99.04	98.22
Al ₂ O ₃	24.29	24.19	–	–	4.50	4.06	3.35	3.23	0.13	0.37	0.20	0.18
MgO	0.00	0.00	0.93	1.07	–	–	–	–	–	–	–	–
FeO	0.00	0.03	1.60	1.70	0.12	0.12	0.20	0.27	0.24	0.11	0.65	0.99
MnO	0.03	0.01	0.09	0.10	–	–	–	–	–	–	–	–
CaO	5.26	5.31	57.01	58.31	29.12	28.92	29.07	28.73	0.16	1.89	0.21	0.21
Na ₂ O	8.70	8.61	0.00	0.00	0.01	0.01	0.01	0.01	0.02	0.03	0.03	0.02
K ₂ O	0.09	0.09	–	–	–	–	–	–	–	–	–	–
Cr ₂ O ₃	–	–	–	–	0.00	0.00	0.02	0.03	0.10	0.04	0.12	0.09
F	–	–	–	–	1.16	1.04	0.72	0.76	–	–	–	–
Total	98.72	99.39	59.63	61.18	99.75	99.31	99.63	99.79	100.78	100.63	100.24	99.71
	Cations per 8 oxygens		Cations per 3 oxygens		Cations per 5 oxygens				Cations per 3 oxygens			
Si	2.72	2.73	–	–	1.02	1.01	1.01	1.01	0.00	0.01	0.00	0.00
Ti	–	–	–	–	0.84	0.86	0.88	0.89	0.99	0.97	0.99	0.99
Al	1.29	1.27	–	–	0.17	0.16	0.13	0.12	0.00	0.01	0.00	0.00
Mg	0.00	0.00	0.02	0.03	–	–	–	–	–	–	–	–
Fe	0.00	0.00	0.02	0.02	0.00	0.00	0.01	0.01	0.00	0.00	0.01	0.01
Mn	0.00	0.00	0.00	0.00	–	–	–	–	–	–	–	–
Ca	0.25	0.25	0.96	0.95	1.02	1.02	1.02	1.01	0.00	0.03	0.00	0.00
Na	0.76	0.75	0.00	0.00	0.00	0.00	0.00	0.00	0.00	0.00	0.00	0.00
K	0.01	0.01	–	–	–	–	–	–	–	–	–	–
Cr	–	–	–	–	0.00	0.00	0.00	0.00	0.00	0.00	0.00	0.00
Cation sum	5.02	5.01	1.00	1.00	3.00	3.00	3.02	3.01	1.00	1.02	1.01	1.01
F ^f	–	–	–	–	0.12	0.11	0.07	0.08	–	–	–	–
An %	24.9	25.3	–	–	–	–	–	–	–	–	–	–
Ab %	74.6	74.2	–	–	–	–	–	–	–	–	–	–
Or %	0.5	0.5	–	–	–	–	–	–	–	–	–	–

m Matrix calcite, *t* calcite at titanite grain boundary, *gb* rutile from titanite grain boundary, *bn* rutile from boudin neck of boudinaged titanite porphyroblast

Plagioclase occurs both as syn-kinematic porphyroblasts (Fig. 3a) up to 10 mm in diameter and as small granoblastic matrix grains. Porphyroblasts are irregularly shaped with embayed grain boundaries and contain abundant inclusions of clinozoisite, quartz, white mica, and thick bands of fine-grained graphite. Clinozoisite inclusions are both euhedral and anhedral in habit. The rims and cores of porphyroblasts have similar compositions of An_{22-27} and An_{24-28} , respectively.

Titanite porphyroblasts are present in discrete horizons within graphite-bearing samples and, locally, are partially enclosed within plagioclase porphyroblasts (Fig. 3b). Titanite porphyroblasts are typically subhedral and range in size from 100 μm to 5 mm in diameter. Most grains contain planar inclusion trails of graphite + quartz \pm calcite, although some grains have sigmoidal inclusion trails (Fig. 3c). Titanite grain boundaries are irregular and grains are mantled by rutile. Locally, titanite grains are boudinaged, with quartz, calcite, rutile, and ilmenite in the boudin necks; other grains are pervasively fractured (Fig. 3c). Fractures extend into the adjacent matrix and are typically filled with rutile, calcite, and quartz. Titanite

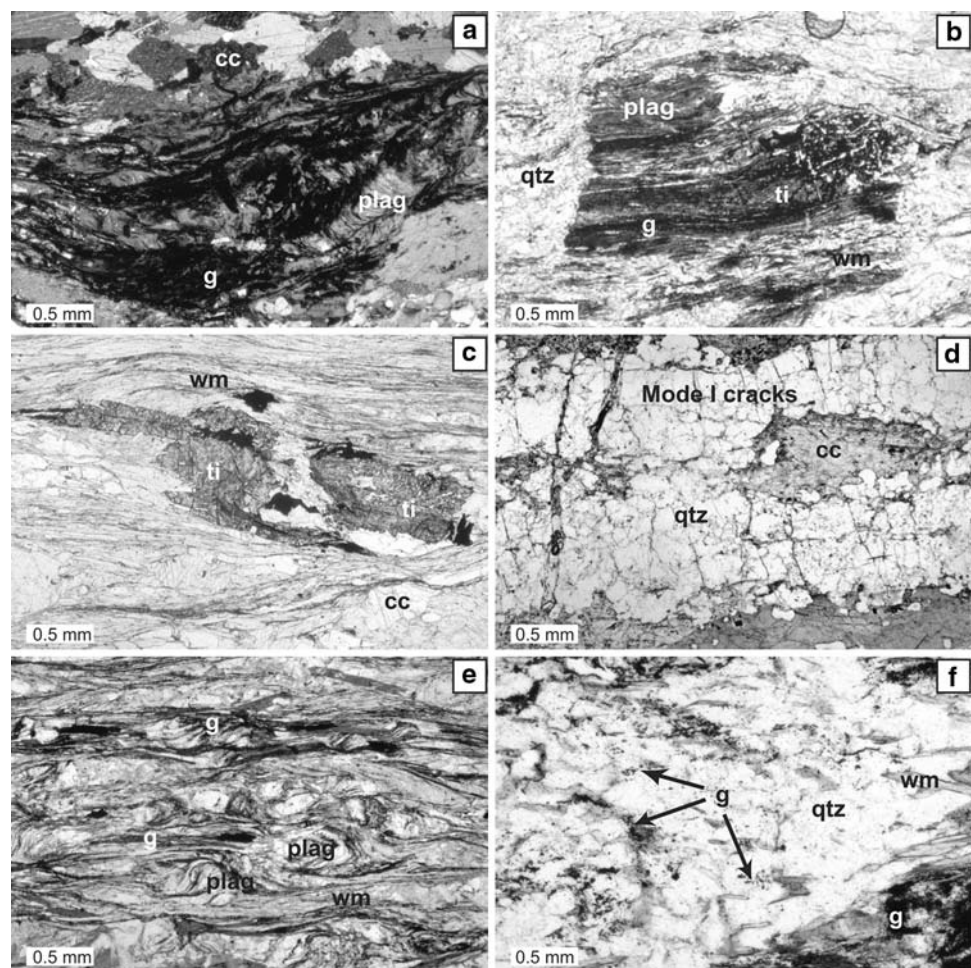
grains contain 0.84–0.89 Ti per formula unit and 0.12–0.17 Al p.f.u. Al contents are positively correlated with Fe (Table 1). Rims are slightly less aluminous than cores.

Rutile occurs in close association with titanite, both along titanite grain boundaries and lining transgranular fractures. Grain morphology varies between prismatic and anhedral. Rutile grains are typically 10–30 μm in diameter, although some grains are up to 100 μm across. Rutile shows no discernable compositional deviation from TiO_2 .

Calcite is present as a principal constituent in the matrix of both graphitic and non-graphitic schists and marbles. Additionally, it occurs in close association with quartz and rutile at titanite grain boundaries and in the necks of boudinaged titanite grains. Analyses of calcite in the matrix and in association with titanite show small but similar concentrations of FeO (Table 1).

Fine-grained *graphite* occurs in black, semi-continuous seams in white mica-dominated horizons. The abundance of graphite from one horizon to another across the foliation is variable and likely reflects primary heterogeneities in organic carbon content. Quartz- and calcite-rich horizons generally lack graphite, although micron-scale graphite is

Fig. 3 Photomicrographs of representative graphitic schists from the Vals Tal (a–d) and Zirogalm (e, f) transects. **a** Asymmetric plagioclase porphyroblast enclosing folded graphite inclusion trails (VT6b). **b** Titanite porphyroblast enclosed within plagioclase, both with abundant graphite inclusions (up to 60 area%); graphite absent in adjacent matrix (VT6a). **c** Boudinaged and asymmetrical titanite porphyroblast with 5–10 area % graphite inclusions; only 2–5 area % graphite in adjacent matrix (VT3). **d** Quartz \pm calcite horizon with abundant Mode I microcracks (VT6a). **e** Syn-kinematic plagioclase porphyroblasts in a matrix of fine-grained plagioclase + white mica \pm biotite \pm quartz; equal modal abundance of graphite within porphyroblasts and matrix (BL1Ba). **f** Matrix quartz with graphite along quartz grain boundaries, microcracks are noticeably absent (BL1Ba). *Plag* plagioclase, *qtz* quartz, *wm* white mica, *cc* calcite, *ti* titanite, *g* graphite



locally present at grain boundaries. Graphite also occurs in planar or crenulated inclusion trails within plagioclase (Fig. 3a), titanite (Fig. 3b, c), and clinozoisite. Typically, graphite inclusions are so abundant that the host porphyroblasts appear black in outcrop and in thin section.

Quartz in horizons with abundant microcracks displays deformation lamellae, undulatory extinction, and sutured grain boundaries. In contrast, quartz in layers without microcracks shows a greater degree of recovery, as evidenced by subgrain development and straighter grain boundaries. Similar observations were made by Selverstone (2005).

Microcracks

On the microscopic scale, Mode I fractures are most prominent in quartz-rich layers separating white mica \pm graphite horizons (Fig. 3d). Although some microcracks are not annealed, most fractures are either preserved as secondary fluid inclusion planes or are filled with fine-grained carbonate. Individual porphyroblasts of titanite, plagioclase, and clinozoisite porphyroblasts in graphitic schists also contain Mode I fractures, which extend into the surrounding matrix where they are defined by secondary fluid inclusion planes.

The abundance of Mode I microcracks in quartz horizons differs between graphitic and non-graphitic schists. Microcrack spacing in samples with a range of modal abundances of graphite in porphyroblasts and matrix was measured perpendicular to the lineation in adjacent quartz horizons. Although some variability in the length and width of the quartz horizons exists, the aspect ratio of the layers was constant at $\sim 10:1$. Five graphitic schists, samples VT1a, VT2a, VT3, VT6a, and VT6b have average crack spacings of 330, 220, 700, 330, and 300 μm , respectively ($\pm 10 \mu\text{m}$). Non-graphitic schists and impure marbles have a lower abundance of Mode I cracks. For example, samples VT2c (non-graphitic schist) and VT4 (marble) have average crack spacing of 5.7 mm and 2.0 mm, respectively ($\pm 500 \mu\text{m}$).

Graphite consumption

Overall graphite abundance varies from sample to sample and likely reflects primary sedimentological heterogeneity. However, differences in the graphite modal abundance within porphyroblasts and in the adjacent matrix, ascertained by visual estimation of graphite distribution, indicates graphite consumption by reaction during or after porphyroblast growth (Although we refer to these estimates as area % graphite, values significantly overestimate the true abundance of graphite because *all* graphite present within a 30 μm thick grain, not just graphite at the surface of the thin section, is visible). For example, sample VT6a

contains up to 60 area % graphite in plagioclase and titanite porphyroblasts (Fig. 3b). The adjacent matrix within the same foliation plane exhibits less than 1 area % graphite. In comparison, sample VT3 contains titanite porphyroblasts with 5–10 area % graphite (Fig. 3c). However, the graphite abundance in the adjacent matrix is only 2–5 area % less than that of the porphyroblasts, suggesting that little graphite was consumed after growth of the porphyroblasts.

Titanite reaction

Titanite porphyroblasts present in graphitic schists are typically rimmed by rutile, calcite, and quartz. Textural observations support the interpretation that titanite partially reacted to rutile, calcite, and quartz in the presence of a carbonic fluid ($\text{titanite} + \text{CO}_2 \rightarrow \text{rutile} + \text{calcite} + \text{quartz}$). Petrographic observations and back-scattered electron (BSE) imaging show that the titanite reaction occurs in three different locations within the titanite grains: (1) along titanite grain boundaries (Fig. 4a, b); (2) as a reaction front oriented perpendicular to the long axis of the titanite grain (Fig. 4a); and (3) in transgranular microcracks that extend from the titanite grains into the adjacent matrix (Fig. 4c).

Zirolalm transect

Graphitic and non-graphitic schists near the Brenner Line have a foliation that strikes between 130° and 175° and dips between 20° and 50° to the WSW. Two lineations are observed, a stretching lineation that plunges shallowly to the WSW (255° – 280°) and a fold axis lineation that plunges shallowly to the SW (225° – 240°). In contrast to the Vals Tal region, macroscopic Mode I fractures occur in both graphitic and non-graphitic layers and range from cracks that are 2 cm in length, 1–2 mm wide, and spaced every 1–6 cm to fractures that are 15–20 cm in length, up to 1 cm wide and filled with altered carbonate, and spaced up to 20 cm (Fig. 2b).

Schists from the Zirolalm transect contain subequal amounts of quartz, plagioclase, biotite (commonly altered to Fe-chlorite), white mica (paragonite), Mg-chlorite, and calcite. Plagioclase locally occurs as porphyroblasts up to 10 mm in diameter, but no other porphyroblast phases were observed. Accessory phases include rutile, zircon, ilmenite, tourmaline, and apatite. Graphite modal abundance is highly variable. Schists with the highest graphite content contain fine-grained graphite along cleavage planes of white mica and chlorite, as inclusions in plagioclase porphyroblasts (Fig. 3e), and at quartz and plagioclase grain boundaries in the groundmass (Fig. 3f). Graphite inclusion bands within plagioclase are folded and display top-to-west

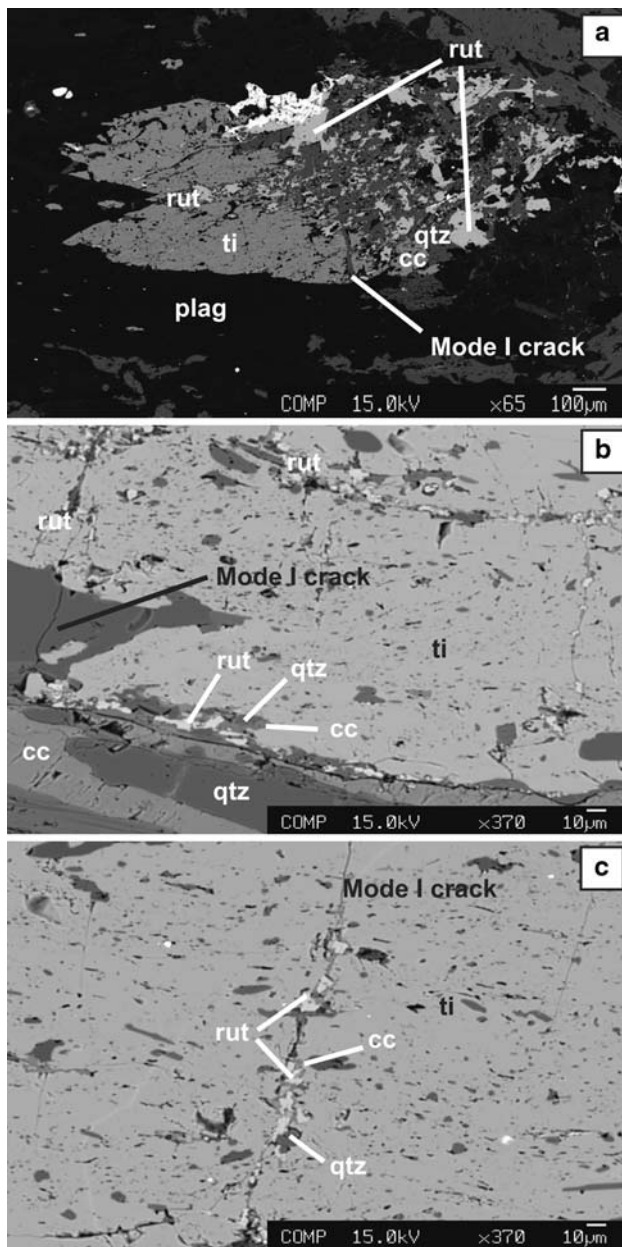


Fig. 4 Back-scattered electron (BSE) images showing titanite breakdown reaction. **a** Titanite porphyroblast partially replaced by rutile, calcite, and quartz (VT6a). **b** Replacement of titanite along Mode I cracks and grain edges (VT6a). **c** Detail of Mode I cracks filled with rutile (VT6a). Abbreviations as in Fig. 3; rut-rutile

shear sense indicating that porphyroblast growth was syn- to post-kinematic with respect to movement in the Brenner Line normal shear zone. There is little to no difference in the modal abundance of graphite preserved within plagioclase porphyroblasts and in the matrix of the same samples, indicating that no graphite consumption has occurred since the time of plagioclase growth.

Most samples from the Zirogalm locality, including those with the highest graphite content and with similar

abundances of graphite in porphyroblasts and in the adjacent matrix, lack pervasive Mode I microfractures (i.e., cracks with sub-millimeter spacing). For example, samples BL1Ca and BL1Ba (Fig. 3e, f) display an average microcrack spacing of 3.7 mm and 11.1 mm, respectively ($\pm 500 \mu\text{m}$). Additionally, these samples contain equant quartz grains that lack undulatory extinction, deformation lamellae, or fluid inclusion arrays. Micro-scale Mode I cracks are locally present in some graphitic schists; in these horizons, quartz exhibits undulatory extinction, deformation lamellae, and sutured grain boundaries. These observations are in striking contrast to graphitic schists from the Vals Tal locality, in which all graphitic samples exhibit microcracks.

Graphite morphology

The JEOL 5800 V scanning electron microscope (SEM) at the University of New Mexico was used to obtain high-magnification, high-resolution images of graphite. A sample from the Vals Tal (VT6a) with petrographic evidence for graphite consumption was compared with a sample from the Zirogalm (BL1Ba), in which matrix graphite is preserved. Samples were prepared by breaking off chips from the original hand samples and coating them with 20 nm of Au–Pd. The chips were placed directly on the sample holder in two orientations, parallel to the foliation and perpendicular to the foliation, and secured to the holder with carbon paint. The SEM was operated with an accelerating voltage of 15 kV, a focused beam with a current of less than 1 nA, and a working distance of 15 mm. Additionally, an Oxford ISIS 300 X-ray analyzer was used to produce X-ray maps of specific regions of the samples. Graphite identification was facilitated by EDS analyses and carbon X-ray maps; maps of aluminum, silicon, and calcium were also collected. The beam diameter of the EDS was commonly greater than the diameter of the graphite grains and thus EDS spectra of graphite contained interferences from elements in other phases.

In both the Zirogalm and Vals Tal samples, graphite occurs as individual grains and aggregates on the surfaces of and in between white mica cleavage planes. However, the morphology of the graphite grains differs between the two samples. In Zirogalm sample BL1Ba, graphite occurs primarily as aggregates of hexagonal to subhedral platelets (Fig. 5a). In contrast, graphite in Vals Tal sample VT6a is anhedral with pitted surfaces, and is typically finer grained than in BL1Ba (Fig. 5b).

Graphite crystallinity has been demonstrated to change as a function of metamorphic grade (e.g. Wopenka and Pasteris 1993), which could affect graphite morphology. However, the difference in P–T histories between the Vals

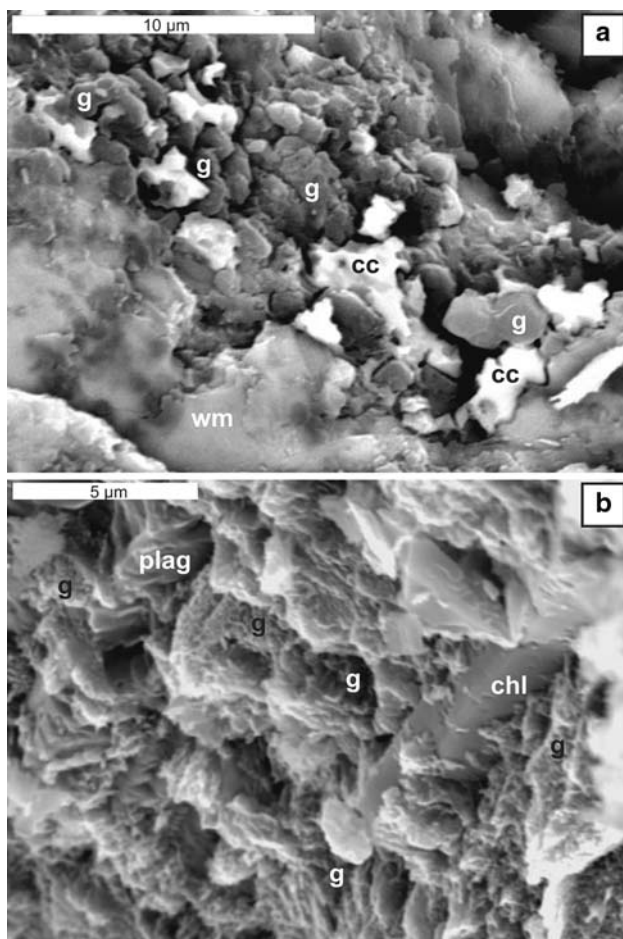


Fig. 5 SEM images illustrating differences in graphite morphology between Vals Tal and Zirogalm graphitic schists. **a** Micron-scale hexagonal graphite platelets and aggregates, intergrown with calcite and interleafed between white mica cleavage planes (VT6a). **b** Graphite on surface of a foliation plane of white mica, plagioclase, and chlorite; graphite is anhedral pitted (BL1Ba). *g* graphite, *cc* calcite, *wm* white mica, *plag* plagioclase, *chl* chlorite

Tal and Zirogalm are unlikely to be large enough (e.g. Selverstone 1985) to explain the difference in graphite morphology observed between the samples. We thus interpret the morphologies in terms of different degrees of graphite consumption via fluid–rock reaction.

Titanite reaction in pressure- X_{CO_2} space

The titanite breakdown reaction can be used to place first-order constraints on fluid composition in the graphitic schists during decompression. Pressure- X_{CO_2} diagrams were generated for graphitic schists from the Vals Tal (samples VT6a and VT3) using the reaction titanite + $\text{CO}_2 \rightarrow$ rutile + calcite + quartz and THERMOCALC software (version 2.75A) with the Holland and Powell (1998) thermodynamic dataset. Titanite activities were calculated for each sample

based on the Ti contents given in Table 1. Activities for rutile, calcite, and quartz were assumed to be unity. Modeling results are thus limited by the variability in titanite composition due to coupled Al-F substitution for Ti–O. Models in P - X_{CO_2} space were generated for temperatures of 450–550°C and pressures of 7–3 kbar, in accord with the P - T constraints determined by Selverstone and Spear (1985) for nearby localities. The results of calculations for isothermal decompression at 500°C are shown here (Fig. 6).

X_{CO_2} in equilibrium with titanite, rutile, calcite, and quartz increases with decreasing pressure, and sample VT6a records slightly higher X_{CO_2} than VT3 along the modeled reaction curve. Although the difference in calculated X_{CO_2} for the two samples is small (between 0.02 and ~ 0.1), sample VT6a shows textural evidence for greater progress of both the graphite- and titanite-consuming reactions compared to VT3.

Early in the unroofing history, syn- to post-kinematic titanite porphyroblasts were stable in rocks with low X_{CO_2} . Samples in which titanite porphyroblasts did not react to rutile + calcite + quartz must plot to the left of the reaction line in P – X_{CO_2} space at any pressure (a in Fig. 6). Partial reaction of titanite buffers X_{CO_2} along the reaction boundary (López Sánchez-Viscaíno et al. 1997) from ~ 0.1 to 0.7 during decompression from 7 to 3 kbar, while simultaneously consuming fluid (i.e., fluid decreases in abundance and also becomes more carbonic). Complete consumption of titanite could allow remaining fluid evolve

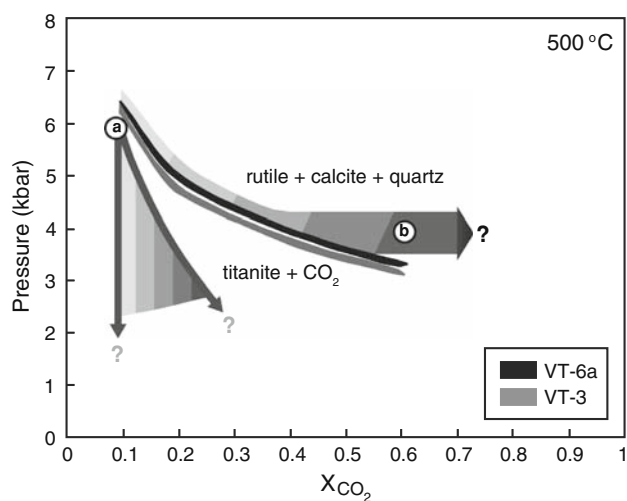


Fig. 6 P – X_{CO_2} diagram for samples VT6a and VT3 based on the titanite reaction and calculated at over the decompression interval of 7–3 kbar at 500°C. Position of titanite reaction denoted by *thick black* and *light gray* lines, reflecting the maximum and minimum titanite activity values calculated from each sample. **a** Titanite is stable throughout unroofing history in rocks with low X_{CO_2} . **b** Generation of CO_2 from graphite consumption drives reaction; as schists are exhumed, X_{CO_2} increases in both samples. If titanite is completely consumed or mantled by reaction products, X_{CO_2} can evolve to higher values

to more carbonic compositions (e.g. via reaction with graphite) at any given pressure (b in Fig. 6).

Metamorphic fluid composition

Information regarding the composition of fluids associated with Mode I cracks was obtained by microthermometric analysis of fluid inclusions in two graphitic samples from the Vals Tal, VT2a and VT3. These samples were selected for microthermometric analyses because they contain quartz-rich horizons with abundant fluid inclusion planes oriented orthogonal to the lineation. Additionally, sample VT3 also exhibits evidence for the titanite reaction, which requires CO_2 to proceed. Fluid inclusion trails in a Mode I orientation are rare to absent in graphitic samples from the Zirogalm transect, so no data could be obtained from this locality for comparison with the VT schists.

Compositions and densities for a total of 174 inclusions were determined using a Fluid Inc. gas-flow heating and freezing stage in the Department of Earth and Planetary Sciences at the University of New Mexico. All samples were initially cooled to temperatures between -100 and -120°C and then warmed while the temperatures of the phase transitions were determined. Depending on the apparent compositional system for each inclusion, the following values were recorded: temperature of initial melting, T_{mi} ; temperature of final melting, T_{mf} (CO_2); temperature of clathrate melting, $T_m(\text{cl.})$; area percent CO_2 vapor relative to co-existing liquid at T_{mf} ; homogenization temperature, T_h [CO_2 liquid–vapor (L–V)]; and percent CO_2 at T_h . Analyzed inclusions were between 4 and 10 μm in diameter. Because

of their small size, it was not possible to observe ice melting in any of the mixed aqueous-carbonic inclusions. Individual temperature measurements were reproducible to $\pm 0.2^\circ\text{C}$. The compositions and densities of entrapped fluids were determined using MacFLINCOR v. 0.77 (Brown and Hagemann 1994) with the Kerrick and Jacobs (1981) equations of state for fluids in the $\text{H}_2\text{O}-\text{CO}_2-\text{CH}_4-\text{NaCl}$ system.

All analyzed inclusions within samples VT2a and VT3 contain mixed $\text{H}_2\text{O}-\text{CO}_2-\text{CH}_4-\text{NaCl}$ fluids. Examples of inclusion geometry and orientation are shown in Fig. 7. In both samples, X_{CH_4} is between 0.00 and 0.06, and NaCl equivalent = 1–3 wt%. X_{CO_2} ranges from 0.08 to 0.81 but most fluid inclusions record values between ~ 0.25 and ~ 0.45 (Table 2). Bulk densities range between 0.51 and 0.96 g cm^{-3} . Inclusions show a correlation between fluid composition and isochoric pressure, with the most H_2O -rich inclusions recording the highest pressures (~ 4.75 kbar) and the most CO_2 -rich inclusions recording the lowest pressures (~ 2 kbar; Fig. 8a, plotted at a reference temperature of 500°C). Graphite-rich horizons in the Vals Tal thus experienced repeated microcracking during decompression from 16.5 to 7 km, coincident with fluid evolution towards increasingly carbonic compositions (Fig. 8b). This pattern is consistent with the observations of Selverstone (2005).

Discussion

Graphite consumption

Petrographic observations comparing porphyroblast and matrix graphite abundance combined with high-resolution

Fig. 7 Photomicrographs of fluid inclusion planes in samples VT2a and VT3. All inclusions contain $\text{H}_2\text{O}-\text{CO}_2-\text{CH}_4-\text{NaCl}$. **a** Mode I fluid inclusion planes in sample VT2a. **b, c** Detail of inclusions from different healed cracks in VT2a; note difference in phase proportions, corresponding to differences in X_{CO_2} and bulk density. **d** Mode I fluid inclusion planes in sample VT3. **e, f** Details of CO_2 -rich inclusions in quartz in VT3

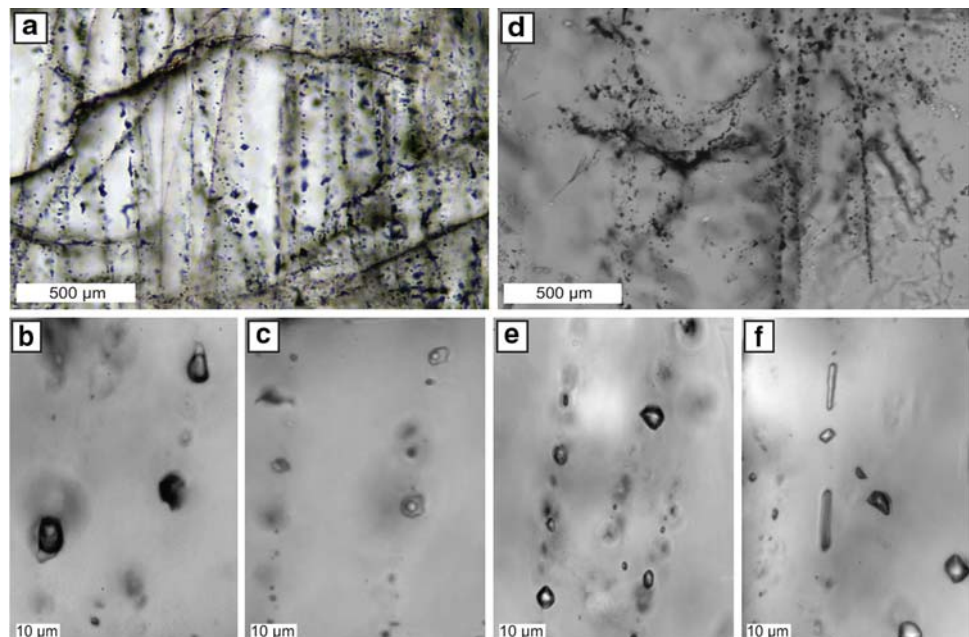


Table 2 Representative fluid inclusion data

Sample	FIA	T_m CO ₂ (°C)	T_m cl (°C)	T_h CO ₂ (°C)	X(H ₂ O)	X(CO ₂)	X(CH ₄)	NaCl eq. (wt%)	Density (g/cm ³)	P (kbar) 500°C
VT2a	Cb-1	-58.0	9.0	24.0	0.56	0.42	0.02	2.0	0.72	2.2
VT2a	Cb-2	-58.3	9.0	24.2	0.53	0.44	0.03	2.0	0.63	1.9
VT2a	Cb-3	-58.2	9.0	24.0	0.85	0.14	0.01	2.0	0.85	3.9
VT2a	Cb-4	-58.4	8.6	24.2	0.65	0.33	0.02	2.8	0.69	2.0
VT2a	Cb-5	-57.9	8.8	24.6	0.67	0.32	0.01	2.4	0.77	2.7
VT2a	Cb-6	-58.4	8.4	23.5	0.71	0.27	0.01	3.1	0.79	2.9
VT2a	Da-1	-57.7	9.1	23.2	0.57	0.42	0.00	1.8	0.70	2.1
VT2a	Da-2	-57.7	8.5	24.6	0.57	0.41	0.02	3.0	0.71	2.1
VT2a	Da-3	-57.5	8.8	25.3	0.67	0.32	0.01	2.8	0.77	2.7
VT2a	Da-4	-58.0	8.8	24.8	0.67	0.31	0.01	2.4	0.76	2.6
VT2a	Da-5	-58.5	8.8	24.0	0.66	0.31	0.02	2.4	0.67	1.9
VT2a	Da-6	-58.1	8.8	24.2	0.63	0.34	0.02	2.4	0.72	2.2
VT2a	Db-1	-58.2	8.6	24.5	0.81	0.17	0.01	2.8	0.78	2.9
VT2a	Db-2	-58.1	8.8	25.4	0.87	0.12	0.01	2.4	0.82	3.4
VT2a	Db-3	-58.2	9.0	23.6	0.90	0.09	0.01	2.0	0.88	4.6
VT2a	Db-4	-58.1	8.4	25.3	0.64	0.34	0.01	3.1	0.71	2.2
VT2a	Db-5	-58.9	9.0	25.1	0.73	0.25	0.02	2.0	0.66	1.9
VT2a	Db-6	-58.2	8.3	24.6	0.69	0.29	0.02	3.3	0.73	2.3
VT2a	Db-7	-57.7	8.4	23.7	0.80	0.18	0.01	4.3	0.87	3.9
VT2a	N-1	-57.9	8.5	24.3	0.78	0.21	0.01	3.0	0.83	3.4
VT2a	N-2	-58.1	8.5	24.0	0.47	0.51	0.02	3.0	0.74	2.3
VT2a	N-3	-57.0	8.8	25.0	0.77	0.22	0.00	2.4	0.85	3.7
VT2a	N-4	-57.4	9.1	25.0	0.60	0.40	0.00	1.8	0.78	2.8
VT3	B-1	-58.7	9.0	16.5	0.63	0.34	0.02	2.0	0.83	3.3
VT3	B-2	-58.8	9.0	15.9	0.83	0.15	0.01	2.0	0.89	4.6
VT3	B-3	-59.0	8.8	13.4	0.46	0.49	0.05	2.4	0.76	2.5
VT3	B-5	-58.9	9.5	12.2	0.51	0.44	0.04	1.0	0.82	3.0
VT3	B-7	-58.8	8.5	15.3	0.14	0.81	0.05	3.0	0.77	2.3
VT3	B-12	-59.0	9.0	11.6	0.52	0.43	0.05	2.0	0.82	3.0
VT3	B13	-58.9	8.7	10.3	0.62	0.35	0.03	2.6	0.88	3.8
VT3	D-2	-59.1	8.8	16.2	0.38	0.56	0.06	2.4	0.74	2.2
VT3	D-3	-58.4	9.0	16.2	0.51	0.46	0.02	2.0	0.82	3.2

Each row is a representative analysis from a set of 4–8 inclusions in a single Mode I fracture. FIA is fluid inclusion assemblage. T_m CO₂, final melting temperature of carbonic phase; T_m cl, clathrate melting temperature; T_h , CO₂ homogenization temperature. All inclusions homogenized to liquid. X(H₂O), X(CO₂), and X(CH₄) are mole fractions referenced to total inclusion (not including salt). NaCl eq. is the wt% salt assuming all salt is NaCl. P at 500°C is the isochore pressure at a reference temperature of 500°C

SEM imaging reveal textural evidence for varying degrees of graphite consumption in some graphitic schists. Hexagonal graphite platelets, such as those observed in Zirogalm sample BL1Ba (Fig. 5a), provide little textural evidence for fluid–graphite reaction, consistent with the similar graphite abundances observed in porphyroblasts and in the matrix at this locality. In contrast, the pitted graphite surfaces observed in VT6a (Fig. 5b), coupled with the decrease in graphite abundance from within porphyroblasts to matrix materials in the same horizon, are consistent with fluid–rock reaction resulting in graphite consumption.

Graphite consumption can result in either the generation of calcite or a carbonic fluid. New calcite growth seems unlikely for samples from the Vals Tal and Zirogalm transects, as it would require available Ca from the breakdown of such phases as plagioclase or clinozoisite. Although graphitic schists analyzed in the present study contain these phases, there is no definitive textural evidence for the breakdown of Ca-bearing minerals. Furthermore, although the unreacted graphite in sample BL1Ba (Fig. 5a) is intergrown with calcite, no calcite is present in association with the pitted graphite in VT6a (Fig. 5b). We thus infer that

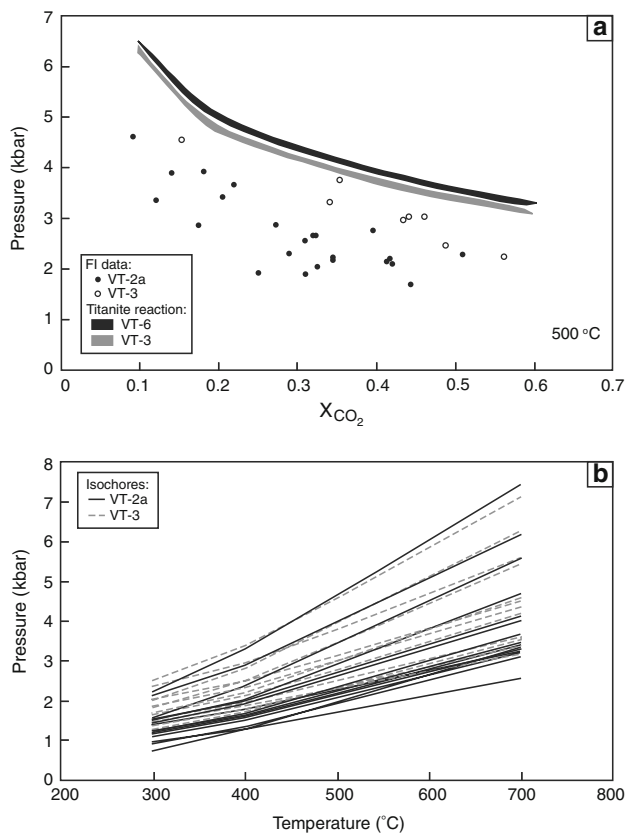


Fig. 8 **a** Isochoric pressure versus fluid composition at a reference temperature of 500°C for Vals Tal graphitic schists; titanite reaction shown for reference. Data points are from Table 2. X_{CO_2} increases with decreasing pressure for both samples. Inclusions in sample VT3 are slightly more carbonic and/or record higher pressures of entrapment at 500°C than those in VT-2a. **b** Corresponding isochores illustrating that repeated microcracking occurred at pressures of ~4.75 to 2 kbar, corresponding to unroofing from ~16 to 7 km

consumption of graphite in the presence of grain boundary fluid resulted in the generation of a carbonic fluid via the generalized reaction $2C + 2H_2O \rightarrow CO_2 + CH_4$. Results of fluid inclusion analyses (X_{CO_2} ranging from 0.1 to 0.8) support this interpretation.

The graphite-consuming reaction suggests that equal proportions of product phases should be produced. However, analyzed fluid inclusions record X_{CO_2} between ~0.1 and 0.8, with negligible CH_4 (Table 2; $X_{CH_4} < 0.06$). Connolly and Cesare (1993) argue that the graphite-saturated C–O–H fluids are typically generated with the maximum thermodynamic activity of H_2O and therefore produce equimolar amounts of CO_2 and CH_4 . However, carbonate-rich graphitic schists are capable of buffering X_O^{fluid} to higher values, which in turn increases the $CO_2:CH_4$ ratio. This latter scenario is applicable to the calcite-rich rocks of this study.

Graphitic rocks that display textural evidence for consumption of nearly all of their original graphite likely

generated the most carbonic fluid. Samples that contain equivalent abundances of graphite in porphyroblasts and in the adjacent matrix likely lacked a pervasive, reactive grain boundary fluid and hence were unable to generate a carbonic fluid. It should be noted that these two scenarios are, in effect, end-members. Within a given sample, the initial amount of graphite preserved in porphyroblasts varies across the foliation, as does the relative amount of graphite consumed during or since porphyroblast growth. Thus, the degree of graphite consumption varies even within a given sample. Our observations imply that reactive grain-boundary fluids were heterogeneously distributed throughout the rocks during metamorphism. Where an aqueous fluid was present, reaction with graphite drove the fluid towards increasingly carbonic compositions during unroofing.

Rheologic and metamorphic implications

A spatial correlation exists between areas where graphite was consumed, yielding a carbonic fluid, and the presence of abundant micro-scale Mode I fractures; this correlation is consistent with the observations of Selverstone (2005). For example, VT6a (Fig. 3b) displays the greatest degree of graphite consumption (based on estimates of graphite abundance within plagioclase porphyroblasts vs. adjacent matrix) and has the most Mode I microcracks (average crack spacing $\approx 330 \mu m$). VT3 (Fig. 3c) shows much less graphite consumption, and has half as many Mode I cracks (crack spacing $\approx 700 \mu m$). No graphite consumption was apparent in the Zirogalm samples (BL1Ba, Fig. 3d, e; BL1Ca); microcrack spacing in these samples is one to two orders of magnitude greater than in the graphite-bearing rocks from the Vals Tal.

In those graphitic schists that contain titanite porphyroblasts, the consumption of graphite to produce a CO_2 -rich fluid served as a catalyst to drive the titanite reaction. The localized occurrence of fine-grained rutile + calcite + quartz partially replacing titanite along grain boundaries and lining Mode I microcracks indicates that a reactive carbonic fluid was present within the matrix and gained access to grain interiors at the time of Mode I cracking.

The graphite- and titanite-consuming reaction boundaries overlap with the fluid inclusion isochores in P–T space (Fig. 9), supporting the hypothesis that the fluid–rock reactions were temporally associated with rock embrittlement (Note, however, that the fluid inclusion data are consistently offset to lower P and/or X_{CO_2} relative to the titanite reaction in P– X_{CO_2} space (Fig. 8). This offset likely reflects the different thermodynamic datasets used by the THERMOCALC and MacFLINCOR software, coupled with uncertainties inherent in fluid inclusion analysis.

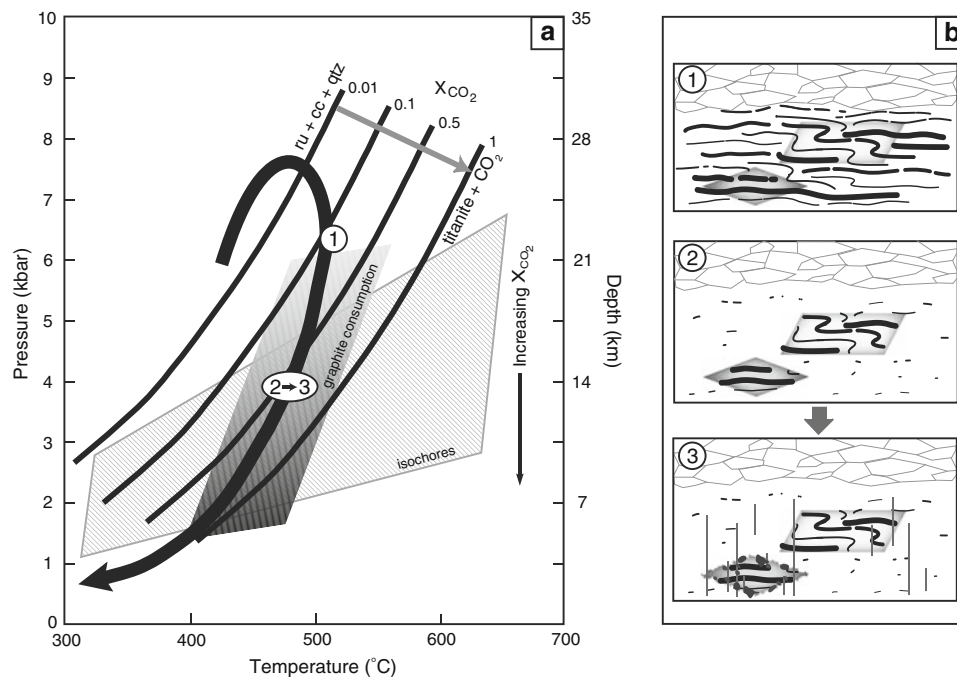


Fig. 9 **a** P–T–depth diagram for Vals Tal USH rocks, showing: position of titanite reaction (black lines) as a function of X_{CO_2} (arrow indicates direction reaction boundary shifts with increasing X_{CO_2}), calculated using THERMOCALC and the thermodynamic dataset of Holland and Powell (1998); isochore range (hatched polygon) for fluid inclusions associated with Mode I microcracks; approximate position of graphite-consuming reaction (gray swath); and P–T path for the USH from Selverstone and Spear (1985). Note that for both the

isochores and graphite-consuming reaction, X_{CO_2} increases with decreasing pressure. **b** Cartoons illustrating fluid–rock reactions and deformation occurring in graphitic schists at different points on the P–T path: (1) X_{CO_2} is low and titanite is stable. (2) Graphite in matrix is partially consumed, increasing X_{CO_2} . (3) The presence of a carbonic fluid triggers formation of Mode I microcracks and destabilizes titanite in favor of rutile + calcite + quartz

Considering these factors, these two datasets are likely within error of one another).

Evolution of the metamorphic fluid composition in graphitic schists is constrained by the titanite reaction curve in $P - X_{\text{CO}_2}$ space and the results of fluid inclusion analyses. However, these data do not shed any light on the amount of fluid present in the graphite-bearing rocks during their unroofing history, which may be an important variable affecting reaction progress and the degree of embrittlement. Ongoing equilibration between graphite and an aqueous grain boundary fluid will produce an increasingly carbonic fluid with decreasing pressure, but does not change the total number of moles of fluid present. However, because CO_2 has a much higher molar volume than H_2O at the relevant P–T conditions (e.g. 44.713 vs. 21.757 $\text{cm}^3 \text{mol}^{-1}$ at 500°C and 4 kbar; Duan and Zhang 2006), this reaction will increase the volumetric fluid–rock ratio, and will also increase pore fluid pressure if permeability is low. In contrast, the titanite reaction results in net consumption of fluid while also changing its composition. Because the titanite reaction cannot proceed in the presence of an aqueous fluid at the P–T conditions of the Vals Tal samples, reaction of graphite with fluid is a necessary

precursor to titanite breakdown. Once titanite consumption begins, however, the fluid composition is buffered to more CO_2 -rich compositions while the net amount of fluid is depleted by one mole of CO_2 per mol of titanite involved in reaction (equivalent to $\sim 0.79 \text{ cm}^3 \text{ CO}_2$ consumed per cm^3 of titanite at 500°C and 4 kbar). As shown by Selverstone (2005), embrittlement of graphitic schists in the area occurred in response to volume expansion of a carbonic fluid, which increased P_{fluid} and triggered extension fracturing. Because Mode I microcracks do not cross titanite reaction products, we hypothesize that the titanite reaction shut down the embrittlement process by using up the available fluid in some of the Vals Tal samples. In other samples, such as VT6a, consumption of all graphite in the matrix limited the rocks' ability to buffer fluid composition to high X_{CO_2} and could have shut off further embrittlement during exhumation.

Source of initial grain boundary fluids

The grain boundary fluid responsible for graphite consumption could have been generated by in situ dehydration of phases such as white mica, clinozoisite, or chlorite, or

could have infiltrated the rocks from an external source. Although it is difficult to distinguish between these two possibilities with certainty, an external fluid origin is more likely for two reasons. First, work by Pattison (2005) indicates that in rocks containing 0.4–1.2 volume% graphite, complete dehydration of ~20% chlorite and ~30% muscovite led to consumption of only 0.1–0.3 volume% graphite—i.e., approximately 25% of the original graphite. The amount of graphite consumed is significantly greater and the amounts of chlorite and muscovite consumed are significantly smaller in the Vals Tal samples than in Pattison's (2005) study, making it unlikely that prograde devolatilization reactions alone were responsible for graphite consumption.

Second, mass balance calculations support the interpretation that the rocks were infiltrated by an initially aqueous, externally derived fluid. A black-shale protolith containing 10 wt% total organic carbon (TOC) will contain approximately 10 volume % graphite when converted to a schist. Removal of 90% of this graphite in the Vals Tal samples corresponds to consumption of 0.017 mol graphite per cm³ of rock. Because the reaction $2C + 2H_2O = CO_2 + CH_4$ consumes 1 mole of water for every mole of graphite, 0.017 mol H₂O must also be consumed per cm³ of rock. At 500°C and 4 kbar, this corresponds to 0.25 cm³ of water for every cm³ of rock involved in the reaction (H₂O specific volume data from Zhang and Duan 2005). Assuming more conservative values of 3 wt% TOC in the protolith and only 50% removal by reaction, ~0.075 cm³ of water would still be needed per cm³ of rock. For comparison, dehydration of 20 volume % muscovite releases just 0.04 cm³ H₂O/cm³ rock at the same conditions, and dehydration of 10 volume % chlorite releases 0.037 cm³ H₂O/cm³ rock. There is no textural evidence to suggest that significant dehydration of these phases occurred during unroofing of the rocks. Based on these numbers, it is clear that in situ dehydration reactions could not have produced enough water to drive consumption of graphite in the Vals Tal samples. Infiltration of significant quantities of externally derived fluid is thus required by the data at this locality.

Structural controls on fluid migration

Petrographic observations indicate that graphite consumption occurred during or after porphyroblast growth, which was contemporaneous with development of the penetrative, mylonitic foliation due to shearing on the Brenner Line detachment (Selverstone 1988; Axen et al. 1995). Movement on the Brenner Line and associated structures may have generated permeability that facilitated fluid infiltration along dynamically maintained, foliation-parallel pathways. If this was the case, however, we might expect

samples from the Zirogalm transect, which sits immediately below the detachment, to show the greatest degree of grain-scale fluid–rock interaction. This is not the case: samples from the Zirogalm transect show little to no evidence of graphite consumption, whereas rocks from the Vals Tal record significant graphite consumption. Key differences in structural style between the localities may have influenced fluid behavior and controlled the degree and type of fluid–rock interaction, and hence also the composition of the fluid.

One difference between the two study sites is the orientation of the dominant mylonitic foliation. In the Vals Tal, the foliation is subvertical to steeply overturned, and this fabric orientation is thought to have been well established prior to the onset of Oligo-Miocene unroofing (e.g. Mancktelow et al. 2001). In contrast, rocks along the Zirogalm transect were transported along the ramp of a major low-angle shear zone, passing through a rolling hinge that steepened dips from sub-horizontal to gently west dipping (Axen et al. 1995), over the same time and depth interval.

The most important difference is that the Zirogalm lies within the region that was strongly affected by rolling hinge deformation during slip on the Brenner Line (Axen et al. 1995). In this area, the foliation is pervasively crosscut by brittle-ductile shears and two generations of high-angle normal faults; these structures were active over the same unroofing interval as the reactions documented in this study. Many of these structures are filled with quartz ± carbonate veins that are riddled with fluid inclusions (Selverstone et al. 1995). There is thus clear evidence for fracture-controlled fluid migration at this locality, but little interaction between these fluids and the surrounding country rock. In contrast, the Vals Tal lies outside of the area affected by rolling hinge deformation and contains relatively few brittle faults. Fluid flow at this locality was likely controlled by grain-scale processes within individual foliation-parallel compositional horizons. Flow may have been facilitated by the subvertical dips in this area, with fluid released at depth channeled upwards in layers of relatively enhanced permeability while adjacent layers saw little to no external fluid.

Mesoscale Mode I fractures are present at both localities, but only the Vals Tal samples show evidence for pervasive cracking on the microscopic scale and a correlation with carbonic fluid generation. Given the proximity of the Zirogalm locality to the Brenner Line, the mesoscale fractures at this site may reflect elevated strain rates while the rocks were transported up the ramp of the shear zone. The fact that microcracks are confined to graphitic horizons in the Vals Tal, however, requires an internal control on embrittlement regardless of external forcing exerted by variations in strain rate (see also Selverstone 2005).

Conclusions

The results of this study show that fluid–rock interactions involving graphite can affect fluid composition, other fluid–rock reactions, and rheology. Interaction between graphite and an aqueous grain boundary fluid yields a carbonic fluid, which can promote embrittlement during exhumation (e.g. Selverstone 2005). Where microcracks transect titanite porphyroblasts, they served as small-scale conduits for mixed H₂O–CO₂ fluids, which drove consumption of titanite to produce rutile, calcite, and quartz. Breakdown of titanite reduced the total volume of grain-boundary fluid present in the rocks, which in turn apparently shut off microfracturing. Positive, then negative, feedbacks thus developed between graphite and titanite consumption and brittle failure of the rocks.

Rocks that lack pervasive, aqueous grain boundary fluids or do not contain graphite or carbonates will not evolve carbonic fluids in situ. These rocks are likely to maintain higher values of f_{H₂O} throughout their metamorphic and deformational history, which will facilitate strain accommodation via dislocation creep and/or dissolution–precipitation creep relative to rock horizons containing more carbonic fluids (Post et al. 1996). In addition, the persistence of graphite in rocks that lack a grain boundary fluid can localize ductile strain via lubrication of grain boundaries and cleavage-parallel slip (e.g. Kretz 1996). Given the evidence for heterogeneous fluid–rock reactions on the scale of millimeters to kilometers, rock rheology is also likely to vary, even within rocks of similar composition.

Acknowledgments Funding for this research was provided by NSF grant EAR-0509937 to JS, and a NSF Graduate Research Fellowship, a GSA Research Grant, and a UNM Wengerd Fund travel grant to AA. Helpful discussions and insight from T. Wawrzyniec, A. Brearley, M. Roy, and J. Tullis, and written comments from Brian Evans and an anonymous reviewer, are greatly appreciated. Thanks to A. Hawkins for field assistance. J. Berlin and M. Spilde are gratefully acknowledged for their support with electron microprobe and scanning electron microprobe analyses.

References

- Axen GJ, Bartley JM, Selverstone J (1995) Structural expression of a rolling hinge in the footwall of the Brenner Line normal fault, eastern Alps. *Tectonics* 14:1380–1392
- Axen GJ, Selverstone J, Wawrzyniec T (2001) High-temperature embrittlement of extensional Alpine mylonite zones in the midcrustal ductile–brittle transition. *J Geophys Res* 106:4337–4348
- Behrmann J (1988) Crustal scale extension in a convergent orogen: the Sterzing-Steinach mylonite zone in the Eastern Alps. *Geodin Acta* 2:63–73
- Bigalke J, Junge A, Zulauf G (2004) Electronically conducting brittle–ductile shear zones in the crystalline basement of Rittsteig (Bohemian Massif, Germany): evidence from self potential and hole-to-surface electrical measurements. *Int J Earth Sci* 93:44–51
- Binu-Lal SS, Kehelpannala KV, Satish-Kumar M, Wada H (2003) Multistage graphite precipitation through protracted fluid flow in sheared metagranitoid, Digana, Sri Lanka: evidence from stable isotopes. *Chem Geol* 197:253
- Bowers TS, Helgeson HC (1983) Calculation of the thermodynamic and geochemical consequences of nonideal mixing in the system H₂O–CO₂–NaCl on phase relations in geologic systems: equation of state for H₂O–CO₂–NaCl fluids at high pressures and temperatures. *Geochim Cosmochim Acta* 47:1247–1275
- Brown PE, Hagemann SG (1994) MacFlinCor: a computer program for fluid inclusion data reduction and manipulation. In: De Vivo BD, Frezzotti ML (eds) Fluid inclusions in minerals: methods and applications. Virginia Polytechnic Institute, Blacksburg, pp 231–250
- Chiodini G, Cardellini C, Amato A, Boschi E, Caliro S, Frondini F, Ventura G (2004) Carbon dioxide Earth degassing and seismogenesis in central and southern Italy. *Geophys Res Lett* 31:16
- Colletini C, Barchi MR (2002) A low-angle normal fault in the Umbria region (Central Italy): a mechanical model for the related microseismicity. *Tectonophysics* 359:97–115
- Colletini C, Barchi M, Pauselli C, Federico C, Piali G (2000) Seismic expression of active extensional faults in northern Umbria (Central Italy). *J Geodyn* 29:309–321
- Connolly JAD, Trommsdorff V (1991) Petrogenetic grids for metacarbonate rocks: pressure–temperature phase-diagram projection for mixed-volatile systems. *Contrib Mineral Petrol* 108:93–105
- Connolly JAD, Cesare B (1993) C–O–H–S fluid composition and oxygen fugacity in graphitic metapelites. *J Metamorph Geol* 11:379–388
- Duan ZH, Zhang ZG (2006) Equation of state of the H₂O–CO₂ system up to 10 GPa and 2,573 K: molecular dynamics simulations with ab initio potential surface. *Geochim Cosmochim Acta* 70:2311–2324
- French BM (1966) Some geological implications of equilibrium between graphite and C–H–O gas phase at high temperatures and pressures. *Rev Geophys* 4:223–253
- Fügensschuh B, Mancktelow NS, Seward D (2000) Cretaceous to Neogene cooling and exhumation history of the Oetztal-Stubai basement complex, eastern Alps: a structural and fission track study. *Tectonics* 19:905–918
- Holland TJB, Powell R (1998) An internally-consistent thermodynamic data set for phases of petrological interest. *J Metamorph Geol* 16:309–343
- Kerrick DM, Caldeira K (1993a) Metamorphic CO₂ degassing and early Cenozoic paleoclimate. *GSA Today* 4:57–63
- Kerrick DM, Caldeira K (1993b) Paleatmospheric consequences of CO₂ released during early Cenozoic regional metamorphism in the Tethyan orogen. *Chem Geol* 108:201–230
- Kerrick DM, Jacobs GK (1981) A modified Redlich–Kwong equation for H₂O, CO₂, and H₂O–CO₂ mixtures at elevated pressures and temperatures. *Am J Sci* 281:735–767
- Kretz R (1996) Graphite deformation in marble and mylonitic marble, Grenville Province, Canadian Shield. *J Metamorph Geol* 14:399–412
- Lammerer B (1988) Thrust-regime and transpression-regime tectonics in the Tauern Window (eastern Alps). *Geol Rundsch* 143–156
- López Sánchez-Viscaíno V, Connolly JAD, Gómez-Pugnaire MT (1997) Metamorphism and phase relations in carbonate rocks from the Nevado-Filábride Complex (Cordilleras Béticas, Spain): application of the Ttn + Rt + Cal + Qtz + Gr buffer. *Contrib Mineral Petrol* 126:292–302

- Mancktelow NS, Stöckli DF, Grollmund B, Müller W, Fügenschuh B, Viola G, Seward D, Villa IM (2001) The DAV and Periadriatic fault systems in the Eastern Alps south of the Tauern Window. *Int J Earth Sci* 90:593–622
- Miller SA, Colletini C, Chiaraluca L, Cocco M, Barchi M, Kaus BJP (2004) Aftershocks driven by a high-pressure CO₂ source at depth. *Nature* 427:724–727
- Morteani G (1974) Petrology of the Tauern Window, Austrian Alps. *Fortschr Geol* 52:195–220
- Nesbitt BE, Mendoza CA, Kerrick DM (1995) Surface fluid convection during Cordilleran extension and the generation of metamorphic CO₂ contributions to Cenozoic atmospheres. *Geology* 23:99–101
- Newton RC, Manning CE (2000) Quartz solubility in H₂O–NaCl and H₂O–CO₂ solutions at deep crust-upper mantle pressures and temperatures: 2–15 kbar and 500–900°C. *64:2993–3005*
- Ohmoto H, Kerrick D (1977) Devolatilization equilibria in graphitic systems. *Am J Sci* 277:1013–1044
- Pattison DRM (2005) The fate of graphite in prograde metamorphism of pelites: an example from the Ballachulish aureole, Scotland. *Lithos* 88:85–99
- Post A, Tullis J, Yund R (1996) Effects of chemical environment on dislocation creep of quartzite. *J Geophys Res* 101:22143–22155
- Radhika UP, Santosh M (1996) Shear-zone hosted graphite in southern Kerala, India: implications for CO₂ infiltration. *J South-east Asian Earth Sci* 14:265–273
- Selverstone J (1988) Evidence for east-west crustal extension in the Eastern Alps: implications for the unroofing history of the Tauern Window. *Tectonics* 7:87–105
- Selverstone J (2005) Preferential embrittlement of graphitic schists during extensional unroofing in the Alps: the effect of fluid composition on rheology in low-permeability rocks. *J Metamorph Geol* 23:461–470
- Selverstone J, Spear FS, Franz G, Morteani G (1984) High-pressure metamorphism in the SW Tauern Window, Austria: P–T paths from hornblende-kyanite-staurolite schists. *J Petrol* 25:501–531
- Selverstone J, Gutzler DS (1993) Post-125 Ma carbon storage associated with continent-continent collision. *Geology* 21:885–888
- Selverstone J, Spear FS (1985) Metamorphic P–T paths from pelitic schists and greenstones in the southwest Tauern Window, Eastern Alps. *J Metamorph Geol* 3:439–465
- Selverstone J, Axen GJ, Bartley JM (1995) Fluid inclusion constraints on the kinematics of footwall uplift beneath the Brenner Line normal fault, eastern Alps. *Tectonics* 14:264–278
- Stampfli GM, Borel GD, Marchant R, Mosar J (2002) Western Alps geological constrains on western Tethyan reconstructions. *J Virt Expl* 7:75–104
- Stöckli DF (1995) Tectonics SW of the Tauern Window (Mauls area, Südtirol). Diploma Thesis, ETH-Zürich, 272 pp
- Wawrzyniec T, Selverstone J, Axen GJ (1999) Correlations between fluid composition and deep-seated structural style in the footwall of the Simplon low-angle normal fault, Switzerland. *Geology* 27:715–718
- Wopenka B, Pasteris JD (1993) Structural characterization of kerogens to granulite-facies graphite: applicability of Raman microprobe spectroscopy. *Am Min* 78:533–557
- Zhang ZG, Duan ZH (2005) Prediction of the PVT properties of water over a wide range of temperatures and pressures from molecular dynamics simulation. *Phys Earth Planet Int* 149:335–354